Height profiles of the ionospheric electron density derived using space-based remote sensing of UV and X ray emissions and EISCAT radar data: A ground-truth experiment

A. Aksnes,[1,2] J. Stadsnes,[1] N. Østgaard,[1] G. A. Germany,[3] K. Oksavik,[4] R. R. Vondrak,[5] A. Brekke,[6] and U. P. Løvhaug[6]

[1]   In this study we have derived height profiles of the ionospheric electron density N_e using remote sensing of UV and X-ray emissions from the Polar satellite and EISCAT radar data. The latter technique gives the most accurate determination of N_e providing a means to ground-truthing the satellite imaging measurements. The UV-emission data are taken from the Ultraviolet Imager (UVI) on Polar, while the X-ray data are measured by the Polar Ionospheric X-ray Imaging Experiment (PIXIE). As UVI yields a far better resolution in time and space than PIXIE, our primary approach involves UVI and EISCAT data. For a substorm event occurring on 24 March 1998, we derive N_{e-UVI} profiles valid in the E region above $\sim$105 km. By comparing with simultaneous $N_{e-EISCAT}$ values, we find that the two techniques match fairly well in many cases. The altitude of maximum electron density is usually below 110 km. A few cases reveal $N_{e-EISCAT}$ maxima in the upper E region (130–150 km), indicating a very soft precipitating electron energy spectrum. During such conditions, we observe the largest discrepancies between the N_{e-UVI} and $N_{e-EISCAT}$ profiles. This may reflect the difficulty of obtaining proper energy characteristics from UV emissions, when the mean electron energy is less than $\sim$2 keV. A recalculation of these N_{e-UVI} values has been performed, requiring that the altitudes of the N_{e-UVI} maximum must match the altitudes of the $N_{e-EISCAT}$ maximum. The results reveal a much better agreement between the two data sets, suggesting that UVI is measuring about the same energy flux as EISCAT. Even though the modified N_{e-UVI} values deviate strongly from the old N_{e-UVI} profiles, the effects on the Pedersen conductance, Σ_P, are insignificant. Also, we find that Σ_{P-UVI} are within ±30% of $\Sigma_{P-EISCAT}$ for 15 of 18 cases, suggesting that remote sensing of UV-emissions provide a fairly reliable tool to monitor the Pedersen conductance. We have investigated a second approach by including PIXIE X-ray data to derive $N_{e-UVI + PIXIE}$ values valid in the whole E region and upper D region. Despite the coarse PIXIE resolution, we observe a fairly good match with the $N_{e-EISCAT}$ profiles. By calculating the Hall and Pedersen conductances, Σ_H and Σ_P, we find that the values derived from satellite imaging measurements are within ±25% of the EISCAT values for all four cases, supporting the space-based remote sensing technique to investigate the ionospheric electrodynamics. The results presented in this study suggest that the procedures developed to derive N_e values from the satellite imaging measurements are reliable. We also find that the N_{e-UVI} and $N_{e-UVI+PIXIE}$ values on average are slightly larger (5 and 13%) than the $N_{e-EISCAT}$ values. These discrepancies may be caused by the difference in resolution between the satellite remote sensing data and the radar data, as smoothing of discrete precipitation may result in an overestimation of N_e.

[1]Department of Physics and Technology, University of Bergen, Norway.
[2]Now at the Florida Space Institute, Kennedy Space Center, Florida, USA.

[3]Center for Space Plasma and Astronomy Research, University of Alabama in Huntsville, Huntsville, Alabama, USA.
[4]Johns Hopkins University Applied Physics Laboratory, Laurel, Maryland, USA.
[5]NASA Goddard Space Flight Center, Greenbelt, Maryland, USA.
[6]Department of Physics, University of Tromsø, Tromsø, Norway.

1. Introduction

[2] Space-based remote sensing of visible, ultraviolet (UV), and X-ray emissions provides a powerful tool to monitor the temporal variations of auroral activity on a global scale. In the last 30 years, several missions equipped with auroral imagers have been flown in space, yielding valuable information about our near-Earth space. A great advantage with the remote sensing technique is that the particle precipitation morphology may be resolved from the satellite imaging measurements, allowing us to study the time development of ionospheric parameters, like the electron density N_e, on a global scale.

[3] Despite the good insight in ionospheric electrodynamics using the remote sensing technique, we must keep in mind that the procedures mentioned above, of first deriving precipitating particle energy spectra and thereafter N_e, are most complicated. Consequently, validation studies are needed to ensure the reliability of the estimated parameters. The most accurate determination of N_e is presumably provided by incoherent scatter radars [*Robinson and Vondrak*, 1994], which clearly suggests that N_e profiles derived from satellite remote sensing data should be compared with N_e using radar measurements. A complication with such ground-truth experiments is the difference in temporal/spatial resolution. Still a number of studies have been performed, supporting various remote sensing techniques. In a study by *Robinson et al.* [1989] measurements of far-ultraviolet (FUV) emissions by the Dynamic Explorer (DE)-1 satellite were compared with ionospheric conductances derived using Chatanika radar data. A good agreement was found between the variations in FUV emissions and the conductances. *Vondrak et al.* [1988] derived height profiles of N_e using X-ray data from the Defense Meteorological Satellite Program (DMSP) F2 satellite. These N_e values were then compared with simultaneously measured N_e using the Chatanika radar, revealing good agreement. A similar conclusion was reached by *Robinson et al.* [1992] comparing N_e profiles derived using FUV emissions from the Polar Bear satellite and measured by the Sondrestrom radar.

[4] In 1996 the Polar satellite was launched to study the regions over the poles of the Earth. The Ultraviolet Imager (UVI) [*Torr et al.*, 1995] and the Polar Ionospheric X-ray Imaging Experiment (PIXIE) [*Imhof et al.*, 1995] on board Polar measure UV and X-ray emissions, respectively. Several studies have estimated the precipitating electron energy spectra using UVI and/or PIXIE measurements [e.g., *Brittnacher et al.*, 1997; *Germany et al.*, 1997; *Lummerzheim et al.*, 1997; *Østgaard et al.*, 2000, 2001, 2002a, 2002b; *Chua et al.*, 2001; *Christensen et al.*, 2003; *Sætre et al.*, 2004]. Of particular interest is the technique used by *Østgaard et al.* [2001], combining UV and X-ray measurements to extend the valid energy range of the derived electron spectra. Such a combination of different remote sensing techniques allows a much better understanding of the auroral dynamics, as the various auroral forms are characterized by different precipitating electron energy spectra [*Robinson and Vondrak*, 1994]. The database established by *Østgaard et al.* [2001, 2002a, 2002b] have been used by *Aksnes et al.* [2002, 2004, 2005] to infer height profiles of N_e and thereafter calculate the ionospheric conductances.

[5] A few studies have examined the energy characteristics derived from UVI and PIXIE data. The procedure used to calculate mean energies from UVI measurements was investigated by *Germany et al.* [2001], revealing an upper limit of 23% for modeling errors. Nonmodeling errors like image processing and Poisson uncertainties have been assigned 3 and 5%, respectively [*Germany et al.*, 1997]. In a study by *Østgaard et al.* [2001], the electron energy fluxes calculated from combined UVI and PIXIE measurements were compared with in situ particle measurements from the DMSP spacecraft. For the electron energy range between 0.09 and 30 keV, *Østgaard et al.* [2001] calculated an average ratio of 1.03 ± 0.6 between the measured and derived energy flux. Despite relatively large differences for some of the data points, the results by *Østgaard et al.* [2001] indicate that the energy characteristics deduced from Polar satellite remote sensing data are reasonable. A complicating issue, though, is the large difference in resolution between the two techniques, which may explain the large standard deviation found by *Østgaard et al.* [2001]. In another comparison study by *Aksnes et al.* [2005], the conductances calculated from UVI and PIXIE measurements were compared with similar conductances derived using a ground-based technique called ''Method of Characteristics'' [*Inhester et al.*, 1992; *Amm*, 1995, 1998; *Sillanpää*, 2002]. A correlation coefficient of 0.57 was found between the two conductance sets. This number may seem low, but a number of complicating factors led *Aksnes et al.* [2005] to conclude that a fairly acceptable agreement had been reached.

[6] The results obtained by *Germany et al.* [1997, 2001], *Østgaard et al.* [2001], and *Aksnes et al.* [2005] are promising, suggesting that the energy characteristics derived from the Polar satellite remote sensing data are reliable. We should be cautious with this conclusion, though, considering the limited statistics and the large discrepancies between some of the data points in the studies mentioned above. As already stated, the most reliable measurements of N_e are probably provided by incoherent scatter radars. *Doe et al.* [1997] used UVI measurements to derive the auroral energy flux. The same quantity was then derived from N_e profiles measured by the Sondrestrom radar. During a 16-min time period from an event on 20 May 1996, *Doe et al.* [1997] found that the total energy flux from the radar measurements agreed to within the ±30% uncertainty of the UVI estimates.

[7] In this study we compare Polar satellite imaging data with measurements from an incoherent scatter radar, similar to *Doe et al.* [1997]. Our approach is different, as we derive height profiles of N_e from UV and X-ray emissions, using the procedures described by *Østgaard et al.* [2001] and *Aksnes et al.* [2002, 2004]. These derived N_e values are then compared with simultaneously measured N_e from the European Incoherent Scatter (EISCAT) radar. In section 2, the two techniques are presented, followed by results (section 3) and discussion (section 4). Finally, we conclude in section 5.

2. Data and Techniques

2.1. N_e From EISCAT Radar Data

[8] In this study we use data from the EISCAT UHF radar in Tromsø, Norway. The incoherent scatter radar technique adopted by EISCAT is considered the most proper method to derive N_e [*Robinson and Vondrak*, 1994]. This procedure

Table 1. EISCAT UHF Radar Beam Directions for the Event on 24 March 1998[a]

Beam Direction	Azimuth	Elevation	Time Resolution
1	133.3°	54.5°	65 s
2	183.2°	77.2°	50 s
3	180.0°	89.9°	80 s
4	166.5°	57.2°	65 s

[a]Azimuth angles of 0° and 90° correspond to geographic north and east respectively. The elevation angle is measured from the horizontal plane and upward.

relies on the transmission of coded pulses of electromagnetic energy that in the ionosphere interact with free electrons through the process of Thomson scattering. Since all target electrons have individual thermal motion the total reflected signal will appear to be incoherent. By decoding the received signal, the power spectrum or the autocorrelation function can be determined, and geophysical parameters like the electron density, the electron temperature, the ion temperature, and the line-of-sight ion drift can be derived from the shape of the spectrum. The EISCAT radars are capable of operating within the altitude range between 50 and 2500 km with a temporal resolution varying from less than a second to tens of minutes and with spatial resolution less than 200 m. However, the EISCAT radars typically operate in a more specific mode that is optimized for the particular geophysical process to be studied.

[9] In this study we have investigated a substorm event on 24 March 1998, when the EISCAT UHF radar was running in a mode known as Common Programme Two (CP2). This is one of several standardized experiments that the EISCAT radars run on a frequent basis to collect data of the ionosphere for the broader international scientific community. These Common Programme modes are well documented, with the purpose to maintain the quality of the data so that data from the same mode of operation can be comparable from year to year and over decades.

[10] During the CP2 operation mode the radar antenna shifts between four different beam directions, according to the specifications listed in Table 1. We note that the integration time varies between 50 and 80 s, giving a total cycle time of 6 min. Further, the $N_{e-EISCAT}$ profiles have a spatial resolution of ∼1 km in the horizontal direction and ∼5 km in altitude.

2.2. N_e From Remote Sensing of UV and X-Ray Emissions
2.2.1. The Ultraviolet Imager (UVI)
[11] The UVI camera on board Polar measures UV emissions, produced when precipitating particles excite the neutral atmosphere through collisions. A filter wheel allows the instrument to select between different UV spectral regions, including emissions within the Lyman-Birge-Hopfield (LBH) band (140–180 nm). By dividing these measurements into LBHS (140–160 nm) and LBHL (160–180 nm), the precipitating electron energy characteristics can be extracted. This is due to a varying amount of absorption by O_2 molecules within the LBH band, peaking at the shortest wavelengths and being much less at longer wavelengths. While the ratio between the two wavelength bands is used to determine the mean electron energy $\bar{E}$, the energy flux P is calculated from LBHL.

[12] Using $\bar{E}$ and P derived from UVI measurements, we can provide the spectral distribution of the precipitating electrons assuming the following exponential form:

$$j_{\exp}(E) = A_{0\,\exp} \cdot \exp\frac{-E}{E_{0\,\exp}}, \qquad (1)$$

where $j_{\exp}$ is the differential electron flux, $A_{0\exp}$ is a proportionality factor, E is the electron energy, and $E_{0\exp}$ is the characteristic electron energy. Alternatively, a Maxwellian distribution may be used:

$$j_{\max}(E) = A_{0\,\max} \cdot E \cdot \exp\frac{-E}{E_{0\,\max}}. \qquad (2)$$

[13] It has been known that the UVI technique of estimating mean energy from the LBH ratio fails to work for precipitating electrons in the energy range of ∼1 keV or less. This is due to the lack of O_2 absorption in the upper atmosphere above 150 km [*Germany et al.*, 1998a], yielding a nearly constant LBH ratio. The results of the present study provide insights on the applicability of UVI-derived energy estimates of mean energy and energy flux, suggesting that the lower energy threshold of 1 keV may be closer to 2 keV.

[14] *Germany et al.* [2001] showed that for mean energies above 10 keV, assuming a nominal 1 erg aurora, almost all the LBHS intensity is absorbed (their Figure 1), limiting the use of the LBHL/LBHS ratio for energies much higher than 10 keV.

[15] On the other hand, energy flux estimates are made from LBHL only and are relatively insensitive to O_2 absorption. (Some shorter wavelength emissions are passed by LBHL, so there is a weak O_2 absorption effect). Consequently, energy flux estimates should be valid from at least 0.2 to 25 keV.

[16] Nominally, the UVI data have a spatial resolution of ∼40 km [*Torr et al.*, 1995], but wobbling of the despun platform on the Polar satellite has degraded this resolution in one direction to ∼360 km. For the UVI operating modes used in this study, we have a temporal resolution of almost 2 min. The reader is referred to work by *Torr et al.* [1995] and *Germany et al.* [1997, 1998a, 1998b] for more details about the UVI camera and the technique used to derive precipitating electron energy spectra.

2.2.2. The Polar Ionospheric X-Ray Imaging Experiment (PIXIE)
[17] The interaction between precipitating electrons and the nuclei of atmospheric particles causes production of X-ray bremsstrahlung. Such X-ray emissions are measured by the PIXIE camera on Polar. The efficient PIXIE X-ray detection range is between ∼2 and 22 keV, allowing an estimation of the precipitating electron spectrum between ∼3 and 100 keV. In this process of obtaining energy characteristics from PIXIE X-ray data, a look-up table based on an electron-photon transport code (developed from neutron transport codes [*Lorence*, 1992]) is used. This look-up table provides values of the X-ray production emitted at different zenith angles for different exponential electron energy spectra. The technique developed (see *Østgaard et al.* [2000] for details) yields a four-parameter spectral distribution of the precipitating electrons.
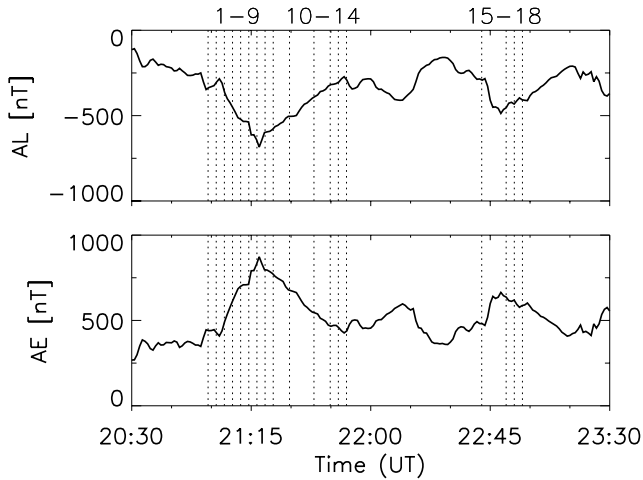
Figure 1. The *AE* and *AL* indices between 2030 and 2330 UT on 24 March 1998. The vertical dashed lines and their respective numbers ranging from 1 to 18 refer to the different times of the plots presented in Figures 2−3.

[18] A great advantage with the PIXIE X-ray technique is that the temporal resolution may be set freely from event to event, not being fixed in time. However, to derive a proper electron spectrum, a sufficient number of detected X-ray photons is needed. This yields an integration time of ∼6 min used in this study, while the spatial resolution is ∼700 km (due to Polar altitude of 7 R_E and the size of the PIXIE pinholes).

2.2.3. Deriving Precipitating Electron Energy Spectra From Combined UVI and PIXIE Measurements

[19] As stated in sections 2.2.1 and 2.2.2, the electron energy characteristics extracted from UVI and PIXIE measurements correspond to different energy ranges. However, by combining these two remote sensing techniques, we can derive precipitating electron energy spectra valid from less than 1 keV to ∼100 keV. A procedure has been developed [*Østgaard et al.*, 2001], in which UVI measurements are averaged within the actual PIXIE time frames and spatial resolution area. The resulting electron energy parameters derived from UVI data are fitted to an exponential and a Maxwellian distribution (equations (1)−(2)). We then choose the UVI-derived spectrum that gives the smoothest transition to the PIXIE-derived spectrum.

2.2.4. Deriving N_e Using MANGLE

[20] A number of studies have investigated the electron transport in the atmosphere [e.g., *Grün*, 1957; *Rees*, 1963; *Mæhlum and Stadsnes*, 1967; *Walt et al.*, 1967; *Banks and Nagy*, 1970; *Nagy and Banks*, 1970; *Banks et al.*, 1974; *Strickland et al.*, 1976; *Vondrak and Baron*, 1976; *Vondrak and Robinson*, 1985; *Solomon et al.*, 1988; *Solomon*, 1989, 1993; *Rees and Lummerzheim*, 1989; *Richards and Torr*, 1990], varying in complexity and reliability. In this study we have used the MANGLE code to calculate the electron density N_e caused by the precipitating electron energy spectra derived from UVI and PIXIE measurements. MANGLE is a relatively simple model, developed by University of Maryland, based on the TANGLE code [*Vondrak and Baron*, 1976; *Vondrak and Robinson*, 1985] and later modified by *Aksnes* [2005]. In the following, we will give a short description on how N_e is calculated using MANGLE.

[21] The ionospheric electron source term q may be derived using the following equation:

$$q(h)dh = \int dE \frac{dF}{dE} \frac{\rho(h)}{\Delta\epsilon_{ion}} [A_{em}(z_m(h)) + A_{xm}(z_m(h))]dh, \quad (3)$$

where h is the altitude, z_m is the atmospheric depth, ρ is the atmospheric mass density, $\frac{dF}{dE}$ is the differential electron current flux, and $\Delta\epsilon_{ion}$ (= 35 eV) is the average energy needed to produce an ion-electron pair. A_{em} is the electron energy deposition function from the cosine-dependent Isotropic over the Downward Hemisphere (IDH) model of *Rees* [1963]. A_{xm} is taken from work by *Berger et al.* [1974] and gives the ionization due to bremsstrahlung X-rays. For additional information about the various parameters listed above, see *Aksnes* [2005].

[22] The electron source term q from equation (3) is related to the electron density N_e through the time-dependent rate equation:

$$dN_e(h)/dt = q(h) + q_0(h) - \alpha_{eff}(h)\cdot N_e^2(h), \quad (4)$$

where q_0 is the background electron source term calculated using the International Reference Ionosphere (IRI)-95 model, and α_{eff} is the effective dissociative recombination coefficient taken from formulas by *Vickrey et al.* [1982] and *Gledhill* [1986]. Note that diffusive transport has not been included into equation (4), as characteristic timescales for diffusion in the *E* region is on the order of hours and days [*Richmond*, 1995a]. Further, we may assume chemical equilibrium, as the recombination time is on the order of seconds around 100 km. This gives $dN_e/dt = 0$, yielding the following expression of N_e:

$$N_e(h) = \sqrt{\frac{q(h) + q_0(h)}{\alpha_{eff}(h)}}. \quad (5)$$

2.3. Event of 24 March 1998

[23] In this study we have derived and compared electron density N_e profiles using the two techniques described in sections 2.1−2.2, during a substorm event occurring on 24 March 1998. The geomagnetic *AE* and *AL* indices between 2030 and 2330 UT are presented in Figure 1. During this 3-hour time period, the geomagnetic disturbances suggest significant substorm activity. While *AL* drops to almost −700 nT (∼2115 UT), *AE* increases to ∼900 nT. This substorm activity takes place during the main phase of a moderate geomagnetic storm, as the *Dst* index drops from ∼0 nT to almost ∼−50 nT within a 12-hour period (not shown here).

[24] The numbers 1−18 and their corresponding vertical dashed lines in Figure 1 indicate the times of the 18 plots presented in Figures 2−3 (section 3).

3. Results

[25] As explained in section 2.2.1, UV emissions provide information about the lower electron energies up to ∼10−
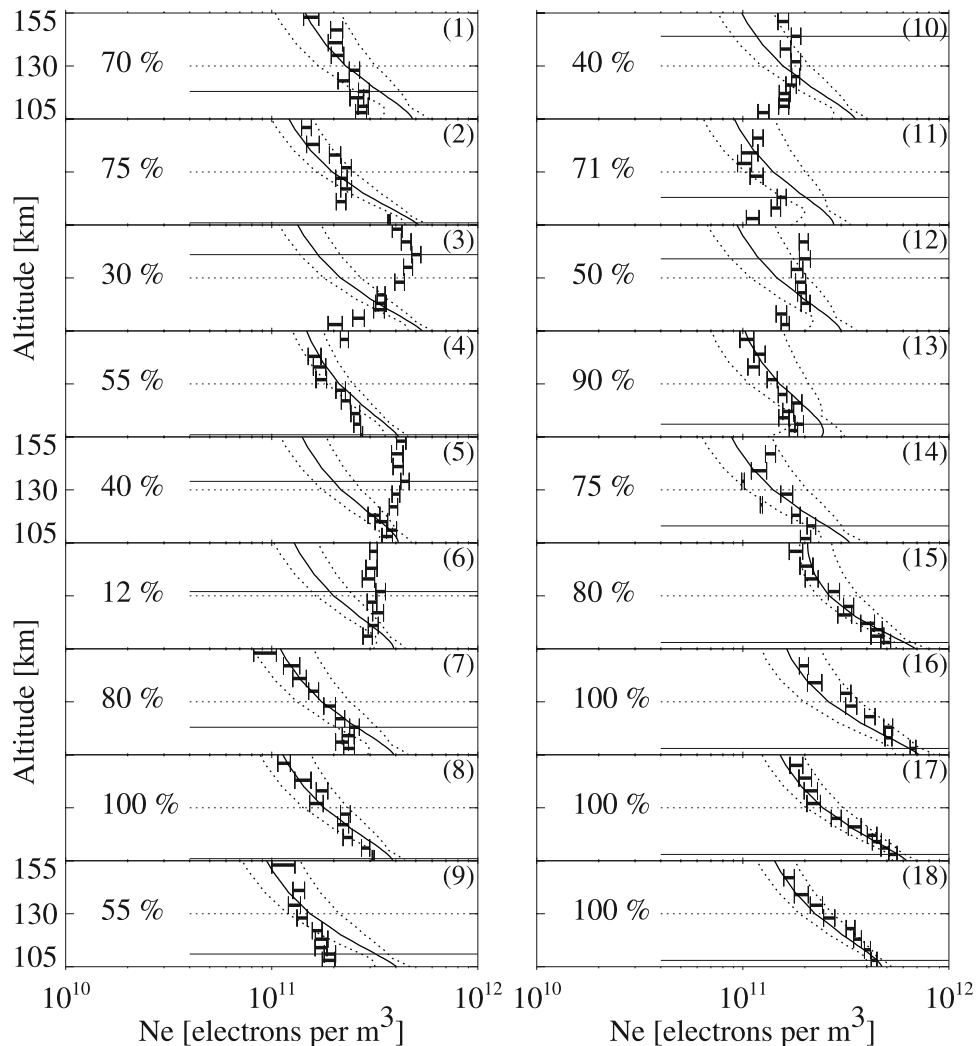
Figure 2. The electron density N_e derived using UVI measurements (solid line) and EISCAT data (horizontal bars) on 24 March 1998. The dashed lines represent the uncertainty of the satellite measurements, and the percentages give the match between the two techniques. The horizontal solid line in each plot indicate the altitude of the $N_{e\text{-}EISCAT}$ maximum, while the horizontal dashed line is plotted at 130 km. The time periods for the plots 1−18 are indicated in Figure 1.

15 keV. To capture the high-energy tail of the precipitating electrons, we also need X-ray measurements (section 2.2.2). While this suggests that both data sets should be included in the comparison analysis, the coarse PIXIE resolution severely complicates a comparison with EISCAT measurements. We have therefore established two different procedures in this study when examining electron density values derived from Polar satellite imaging data. The first approach includes UV emissions only, yielding N_{e-UVI} profiles valid in the E region above ∼105 km (section 3.1). Then we have included PIXIE measurements (section 3.2), resulting in $N_{e-UVI+PIXIE}$ values in the whole E region and upper D region.

3.1. N_{e-UVI} Versus $N_{e-EISCAT}$

[26] The first investigation is a comparison between electron density values derived from UVI measurements, N_{e-UVI}, with similar $N_{e-EISCAT}$ profiles using EISCAT radar data. The values of mean energy and energy flux derived from UVI are represented using an exponential and a Maxwellian distribution. Then we have chosen, in each case, the spectrum which yields the best match between N_{e-UVI} and $N_{e-EISCAT}$. The altitude region of interest goes from 105 to 155 km.

[27] The comparison is complicated by the differences in temporal resolution. It takes about 2 min to perform an energy analysis for the UVI operating mode in this study, while the $N_{e-EISCAT}$ profiles have an integration time varying between 50 and 80 s (Table 1). We have compared each set of N_{e-UVI} values with the $N_{e-EISCAT}$ profile closest in time.

[28] Another difficulty arises from the difference in spatial resolution. While UVI cannot resolve structures less than ∼40 km (section 2.2.1), EISCAT gives N_e profiles in the range of ∼1 km (section 2.1). As EISCAT looks in four different directions during the CP2 mode on 24 March 1998 (Table 1), the EISCAT measurements cover a geographic region of 68.8−69.6° in latitude and 19.2−21.2° in longitude. The N_{e-UVI} profiles used in this study are taken from a larger region surrounding the EISCAT beam locations and
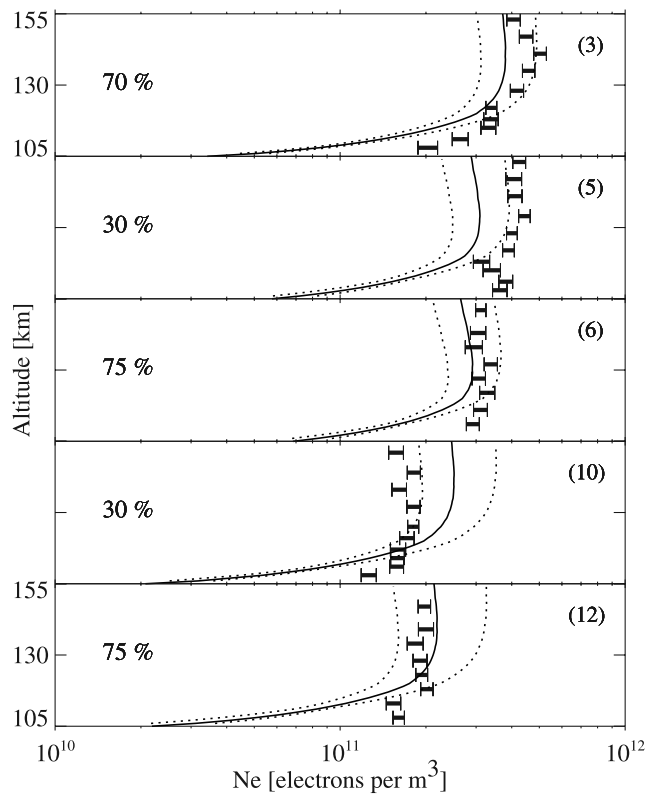
Figure 3. Modified profiles of N_{e-UVI} (solid line) for the five plots in Figure 2 where the $N_{e-EISCAT}$ values (horizontal bars) reveal maxima above 130 km. The dashed lines represent the uncertainty of the satellite measurements.

corresponding to an area of $\sim$100 km $\times$ 150 km. This larger region, exceeding the UVI nominal resolution of $\sim$40 km, is chosen to get sufficient count rates to derive reliable electron energy characteristics.

[29] The difference in resolution suggests that discrepancies are expected to occur when we have discrete precipitation within the UVI field of view (FOV). To minimize such effects, we have performed an investigation of the individual UVI pixel intensities within the UVI region of $\sim$100 km $\times$ 150 km. Only cases where all the individual UVI pixel intensities are within $\pm$50% of the UVI mean value are included in the comparison analysis. The procedure performed is similar to the one described by *Aksnes et al.* [2005], meaning that we only include cases with relatively uniform precipitation within the UVI analysis area.

[30] In Figure 2 we give height profiles of the electron density N_e derived using UVI measurements (solid lines) and EISCAT data (horizontal bars), during the 18 time periods when the particle precipitation is relatively uniform in a larger region surrounding the EISCAT FOV. The length of the horizontal bars gives the $N_{e-EISCAT}$ uncertainties, while the dashed lines represent the N_{e-UVI} uncertainties. The latter have been calculated using the standard deviation of the UVI mean energy and the energy flux. A value is presented in each plot, giving the percentage number of EISCAT data points that fall within the UVI error limits. From Figure 2 we see that some of the data sets reveal a pretty good match between the two techniques, e.g., in plots

16–18 we find that all the $N_{e-EISCAT}$ values are within the N_{e-UVI} uncertainties (100%).

[31] Other plots reveal significant discrepancies between the two techniques. In particular, the profiles deviate strongly in cases where $N_{e-EISCAT}$ shows a maximum in the upper E region. The horizontal solid line in each plot gives the altitude of the $N_{e-EISCAT}$ maximum. Usually, we find the largest $N_{e-EISCAT}$ values below 110 km. However, in plots 3, 5, 6, 10, and 12, the maximum in $N_{e-EISCAT}$ takes place above 130 km (indicated by the horizontal dashed line). As pointed out in section 2.2.1, the lack of O_2 in the upper atmosphere yields an almost constant LBHL/LBHS ratio, meaning that the UVI technique may fail to work. For these five cases in Figure 2 with $N_{e-EISCAT}$ maxima above 130 km, the values representing the match between the two techniques vary from 12 to 50%. In comparison, the remaining 13 plots have corresponding values of match between 55 and 100%.

[32] We have recalculated N_{e-UVI} for the cases when EISCAT data indicate a dominance of lower electron energies, using the following approach: First, we determine the characteristic energy E_0 (equations (1)–(2)) from the peak value of $N_{e-EISCAT}$. Note that this procedure is complicated by the relatively constant N_e values as a function of altitude for plots 5, 6, 10, and 12. This suggests that the chosen peak values, determined by identifying the altitudes with the largest N_e values, are associated with a significant degree of uncertainty. The next step in our procedure is to modify the corresponding value of A_0, keeping the UVI electron energy flux P fixed at the same value as earlier (derived from the UVI-LBHL measurements). P may be expressed:

$$P(E) = \int_{0.1}^{30} j_E \cdot E dE, \qquad (6)$$

where j_E is taken from equations (1)–(2).

[33] In Figure 3 we have replotted the five plots from Figure 2 when the $N_{e-EISCAT}$ values reveal their maxima in the upper E region above 130 km, using the modified height profiles of N_{e-UVI}. This new approach clearly gives a much better agreement between the two techniques, showing that UVI measures about the same energy flux as EISCAT in the upper E region. From Figure 3, we note that the number of points with match between N_{e-UVI} and $N_{e-EISCAT}$ exceed 70% in three of the plots.

3.2. $N_{e-UVI+PIXIE}$ Versus $N_{e-EISCAT}$

[34] As demonstrated by *Aksnes et al.* [2002, 2004], the PIXIE X-ray data are needed to capture the high-energy tail of the precipitating electrons, depositing their energy in the lower E region (below $\sim$105 km) and upper D region. Such X-ray data are available between $\sim$2100 and 2125 UT on 24 March 1998. Within this time period, we have derived electron spectra from PIXIE using a time resolution of 6 min. All available UVI energy parameters within the PIXIE time intervals have been averaged, yielding $N_{e-UVI+PIXIE}$ profiles valid between $\sim$75 and 155 km altitude. Also, note that the given time period of $\sim$2100–2125 UT involves the modified UVI plots 3, 5, and 6 from Figure 3. In Figure 4 the four $N_{e-UVI+PIXIE}$ profiles (solid thin line) are compared with similar 6-min averaged $N_{e-EISCAT}$ values (solid thick line).
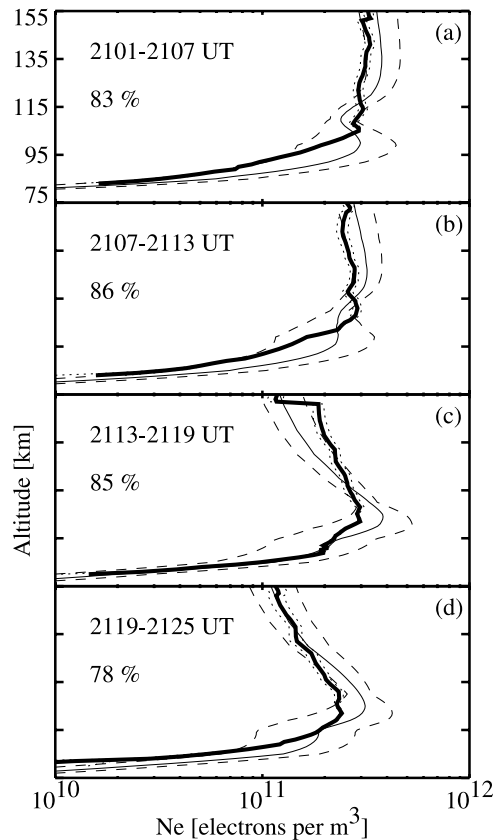
Figure 4. The electron density N_e derived using UVI and PIXIE measurements (solid thin line) and EISCAT data (solid thick line) on 24 March 1998. The dashed and dotted lines indicate the uncertainties of the satellite and radar measurements, respectively.

The PIXIE pixel size of $\sim$700 km is too large to allow an accurate comparison with EISCAT measurements. Still, we find that the two techniques give results that match fairly well. As shown in Figure 4, most of the $N_{e-EISCAT}$ data points (78 to 86%) are within the dashed lines indicating the uncertainties of the satellite remote sensing measurements.

4. Discussion

[35] Space-based remote sensing of UV and X-ray emissions provide a powerful tool to investigate the ionospheric electrodynamics. In this study we have performed a ground-truth experiment of the electron density values N_e derived from UVI and PIXIE measurements, by comparing with simultaneously measured N_e using EISCAT radar data.

[36] To reduce errors caused by the difference in spatial resolution between the two techniques, we have excluded cases with discrete precipitation. As shown in Figure 2, many of the plots reveal a good agreement between N_{e-UVI} and $N_{e-EISCAT}$. Still, large discrepancies may sometimes be observed. This is to be expected, as finer structures in the auroral dynamics will be effectively smoothed out in the satellite imaging data. Therefore randomly distributed deviations should occur from time to time. However, the results presented in Figure 2 also reveal a systematic dominance of $N_{e-EISCAT}$ over N_{e-UVI} in the upper E region during times

when the maximum in $N_{e-EISCAT}$ takes place above 130 km. Ionization maxima at these high altitudes suggest that large parts of the electron precipitation are soft particles of energy $\sim$2 keV or less [*Rees*, 1963]. Such conditions are not favorable when extracting the energy characteristics from UVI measurements. The reason is that the UV technique relies strongly on O_2 absorption of UV emissions, which drops significantly at higher altitudes. We therefore suggest that the discrepancies revealed in plots 3, 5, 6, 10, and 12 in Figure 2 is caused by inaccurate E_0 values derived from UVI data. A special approach is performed for these five cases, where height of the peak value of $N_{e-EISCAT}$ yields a new value of the characteristic energy E_0 for the UVI spectrum (equations (1)–(2)). We then adjust A_0 accordingly, given that the UVI energy flux derived from UVI-LBHL measurements is correct. The results found show that UVI is measuring more or less the same energy flux as EISCAT.

[37] One may think that a possible explanation for the observed differences may be systematic errors in the radar measurements. A bad radar system constant will scale the entire electron density profile at all altitudes, either giving too high or too low electron density values. However, the general shape of an electron density profile from a bad system constant would still be the same as for the true electron density profile. The observations presented in Figure 2 show that most EISCAT profiles align pretty well with the UVI profiles both when it comes to shape and electron density. The few EISCAT profiles that really differ from the UVI profiles generally do not match at all when it comes to the shape of the profile, and this is not at all indicative of a systematic error. It is therefore our opinion that the EISCAT data used in this study are not significantly affected by any systematic errors and that the real uncertainty of the EISCAT data is reflected by the statistical errors of the measurements plotted with error bars in the figures.

[38] The inclusion of PIXIE X-ray measurements in Figure 4 allows us to study a wider altitude range of 75–155 km. The discrepancy in spatial resolution means we must be cautious when interpreting the results, as the PIXIE pixel size is too large to make an accurate comparison with EISCAT data. Still, we find a good match in all four plots, supporting the technique used to derive N_e from satellite remote sensing measurements. Figure 4c (between 2113 and 2119 UT) actually reveals almost identical N_e profiles in the lower E region and upper D region.

[39] In Figure 5 we have calculated the Pedersen conductances, Σ_P, using the 18 N_{e-UVI} (plus symbol) and $N_{e-EISCAT}$ (diamond symbol) profiles presented in Figure 2. A fairly good match is revealed in both trend and magnitude. The pluses in the bottom panel of Figure 5 indicate how much the Pedersen conductances calculated using UVI measurements, Σ_{P-UVI}, differ from $\Sigma_{P-EISCAT}$. For 15 of the 18 cases, the two sets of values are within $\pm30\%$. Also, we find that despite the large altitude variation (Figures 2–3) the five modified N_{e-UVI} profiles yield Pedersen conductance values (triangle symbol) similar to the original N_{e-UVI} profiles (as they almost cover the corresponding pluses). This finding suggests that UV-emissions may be a reliable tool to monitor the Pedersen conductance even during periods when soft precipitation complicates the estimation of the mean electron energy.
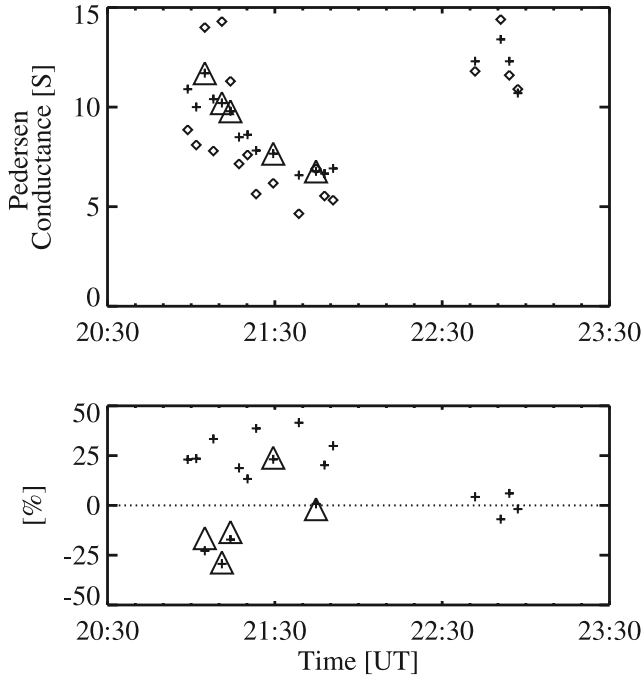
Figure 5. (top) The Pedersen conductances calculated using the 18 $N_{e\text{-}UVI}$ (plus symbols) and $N_{e\text{-}EISCAT}$ (diamond symbols) profiles from Figure 2. Also plotted are the five modified $N_{e\text{-}UVI}$ (△) data sets from Figure 3. The deviations between the two techniques (given in percent) are given in the bottom panel.

[40] The UV technique allows only a two-parameter spectral distribution of the precipitating electrons to be determined. This can explain the apparent underestimation of N_{e-UVI} values at lower heights in Figure 3, where the Hall conductance is significant. Earlier studies by *Aksnes et al.* [2002, 2004] have concluded that X-ray data are needed to derive accurate values of the Hall conductance, as the X-ray photons can be used to capture the high-energy tail of the precipitating electrons. This is most important because the precipitating electron energy spectrum often changes shape and flatten out at higher energies. The Hall and Pedersen conductances calculated using the four $N_{e-UVI\,+\,PIXIE}$ (solid lines) and $N_{e-EISCAT}$ (dashed lines) profiles from Figure 4 are presented in Figure 6, revealing a fairly good match between the two conductance sets. While $\Sigma_{P-UVI\,+\,PIXIE}$ is within ±20% of $\Sigma_{P-EISCAT}$, we find that $\Sigma_{H-UVI\,+\,PIXIE}$ is ~2 to 26% larger than $\Sigma_{H-EISCAT}$.

[41] From the results found in this study, we may argue that remote sensing of UV and X-ray emissions provide a powerful tool to investigate the ionospheric electrodynamics. Still, Figures 4 and 6 indicate that N_e derived from space-based remote sensing is slightly larger than $N_{e-EISCAT}$. A similar tendency is seen in Figures 2 and 5.

[42] By calculating the total height-integrated electron density N_e^T using the profiles presented in Figures 2, 3, and 4, we find a pretty good match between the data sets. However, a closer look at the data reveal that N_{e-UVI}^T and $N_{e-UVI\,+\,PIXIE}^T$ are usually slightly larger than $N_{e-EISCAT}^T$. The 18 $N_{e-UVI}^T/N_{e-EISCAT}^T$ ratios presented in Table 2 yield an average value of 1.05, while the 4 $N_{e-UVI\,+\,PIXIE}^T/N_{e-EISCAT}^T$ ratios give a similar value of 1.13. This moderate overesti-

mation may be due to the large differences in spatial resolution, causing gradients in the precipitation to be smoothed when using the remote sensing technique. Even though we include only cases where the precipitation is relatively uniform, the UVI (PIXIE) resolution of ~40 km (~700 km) means that structures of less spatial extent cannot be revealed. Instead such structures are smoothed. This may result in an overestimation of the electron density. Assume we divide a region of interest in n subregions. In situation 1, we have a very localized precipitation so that the total electron production rate Q_e takes place within one of the n subregions. For this subregion, $N_e = \sqrt{\dfrac{Q_e}{\alpha}}$. As $N_e = 0$ in the other $(n - 1)$ subregions, the $\overline{N_e}$ averaged over the whole region is

$$\overline{N_e} = \frac{1}{n}\sqrt{\frac{Q_e}{\alpha}}. \tag{7}$$

In situation 2, we now assume that the same total electron production rate Q_e as in situation 1 takes places homogeneously over the whole region, meaning that the electron production rate is Q_e/n within each of the n subregions. This results in a larger $\overline{N_e}$:

$$\overline{N_e} = \frac{1}{\sqrt{n}}\sqrt{\frac{Q_e}{\alpha}}. \tag{8}$$
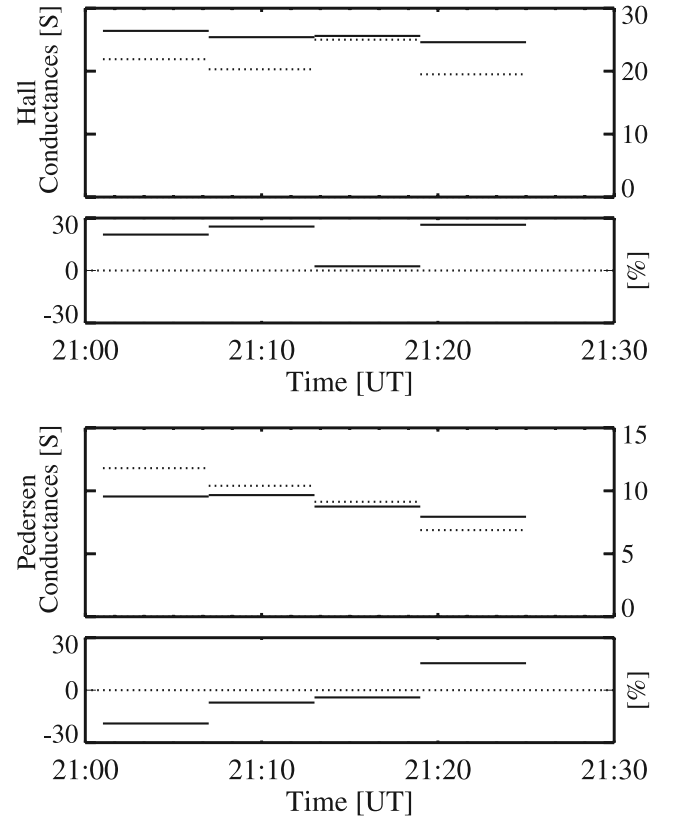
Figure 6. (top) The Hall and (bottom) Pedersen conductances calculated using the four $N_{e\text{-}UVI\,+\,PIXIE}$ (solid lines) and $N_{e\text{-}EISCAT}$ (dashed lines) profiles from Figure 4. Also plotted are the deviations (given in percent) between the two techniques.

Note that the same arguments also goes for differences in temporal resolution. We should add that for small auroral features and large field-of-view per pixel, a number of complicating issues may exist. The problems with differences in spatial resolution, as described above, is only one piece of the puzzle. However, a properly evaluation of these issues is beyond the scope of this paper.

[43] As shown in this study, LBH measurements provide fairly reliable electron density profiles for most of the E region, given mean electron energies between $\sim$2 and 10 keV. During conditions with a very soft precipitation present, though, other remote sensing techniques are needed. In the work of *Strickland et al.* [1983], the intensity of selected visible and FUV emissions as a function of the Maxwellian characteristic energy (their Figure 7) is given. While the 127.3 nm emissions are almost unattenuated regardless of the altitude at which the energy is deposited, the 135.6 nm emissions reveal a strong dependence with mean energy. This suggests that simultaneous measurements of 127.3 and 135.6 nm emissions could be used to infer the low-energy electrons below $\sim$2 keV. In the work of *Robinson and Vondrak* [1994], they show that the ratio between 127.3 and 135.6 nm emissions is proportional with the mean electron energy from a few hundred eV to more than 10 keV. Another approach is proposed by *Semeter et al.* [2001], suggesting to use two spectral bands in the visible region (centered at 427.8 and 732.5 nm) to characterize the precipitating electrons below 1 keV. The remote sensing technique relies on steady-state conditions when solving the continuity equation (equation (5)), and at high altitudes (above $\sim$150 km) the electron density may not reach its steady-state values. Consequently, we may experience differences between N_e derived from satellite data and $N_{e-EISCAT}$, even though the energy characteristics extracted from the satellite measurements are indeed correct.

5. Conclusion

[44] In this study we have performed a ground-truthing of N_e derived from satellite imaging measurements of UV and X-ray emissions, by comparing height profiles of N_{e-UVI} and $N_{e-UVI + PIXIE}$ with $N_{e-EISCAT}$ values using the EISCAT UHF radar in Tromsø, Norway. For a substorm event occurring on 24 March 1998, we have investigated 18 N_{e-UVI} and $N_{e-EISCAT}$ profiles between 105 and 155 km from time periods when the particle precipitation is relatively uniform in a larger region surrounding the EISCAT radar facility. Many of the profiles reveal a good match, supporting the validity of the space-based technique. The largest discrepancies occur during time periods when the $N_{e-EISCAT}$ values indicate that a significant portion of precipitating electrons is in the energy range of $\sim$2 keV or less. We argue that the derived N_{e-UVI} profiles are not valid during such conditions, as the UV-emissions produced in high altitudes are hardly absorbed by O_2. Consequently, the UV-technique used to derive an auroral average electron energy fails to work. A recalculation of the N_{e-UVI} profiles using information of the height of the maximum in N_e from EISCAT radar measurements reveals that UVI is measuring more or less the same energy flux as EISCAT. Despite the difficulties in obtaining a proper height profile of N_{e-UVI}

Table 2. Ratios Between Total Height-Integrated Electron Density Values Using the Profiles Presented in Figures 2–4

Profile	Ratio
Figure 2: $N_{e-UVI}^T / N_{e-EISCAT}^T$	
(01)	1.19
(02)	1.08
(04)	1.15
(07)	1.17
(08)	1.06
(09)	1.35
(11)	1.40
(13)	1.18
(14)	1.16
(15)	1.07
(16)	0.89
(17)	0.99
(18)	0.94
Figure 3: $N_{e-UVI}^T / N_{e-EISCAT}^T$	
(03)	0.79
(05)	0.65
(06)	0.84
(10)	1.13
(12)	0.92
Figure 4: $N_{e-UVI+PIXIE}^T / N_{e-EISCAT}^T$	
(a)	1.17
(b)	1.16
(c)	1.00
(d)	1.19

during time periods with soft precipitation, the effects on the Pedersen conductances Σ_P turn out to be insignificant. A comparison with EISCAT calculations further shows that Σ_{P-UVI} are within $\pm$30% of $\Sigma_{P-EISCAT}$ for 15 of 18 cases, indicating that UV emissions are a powerful tool to examine the Pedersen conductance.

[45] The inclusion of PIXIE X-ray data in the comparison analysis has extended the satellite-derived N_e profiles to include the lower E region and upper D region. The analysis performed cannot be considered an absolute validation of the value of the combined UV/X-ray method. This is due to the large PIXIE pixel size, preventing an accurate comparison with EISCAT data. The technique presented should work fine, though, if X-ray measurements with a much higher spatial resolution were available. Still, the results are promising, showing relatively good match between $N_{e-EISCAT}$ and $N_{e-UVI + PIXIE}$. We further find a pretty good match (within $\pm$25%) when calculating the Hall and Pedersen conductances using the two techniques.

[46] An investigation of the total electron density values N_e^T reveals that the satellite imaging measurements give slightly larger values than the ground-based EISCAT data. This may be explained by the difference in resolution, as smoothing of discrete precipitation should yield a larger value of N_e. While N_{e-UVI}^T is 5% larger than $N_{e-EISCAT}^T$, this number increases to 13% when including PIXIE X-ray measurements.

[47] To summarize our result, we show in Figure 7 the validity of remote sensing techniques as a function of altitude of peak energy deposition. During periods with a mean electron energy $\bar{E}$ between 2 and 10 keV, corresponding to peak energy deposition within an altitude region of $\sim$105–130 km [*Rees*, 1963], the UVI technique yields a fairly good determination of the electron density in the whole E region down to 100 km. At lower altitudes,
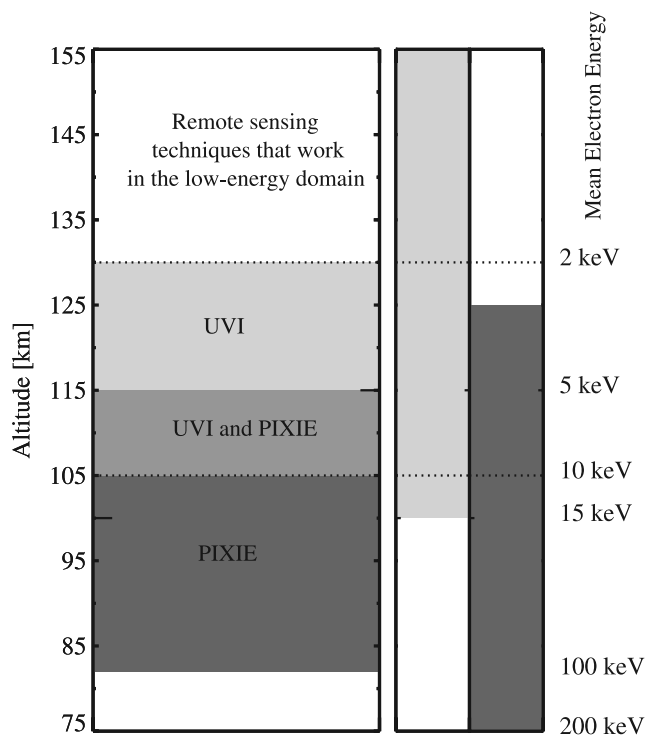
Figure 7. The validity of UVI and PIXIE measurements to determine the electron precipitation as a function of altitude of peak energy deposition. (left) The UVI technique works for mean electron energies $\bar{E}$ between $\sim$2 and 10 keV, while PIXIE data captures the high-energy tail of the precipitating electrons. A transition altitude region exists for heights between 105 and 115 km, where both techniques work properly. Other remote sensing techniques are needed for conditions with $\bar{E}$ below 2 keV. (right) The derived electron spectra from UVI are valid in the upper E region above $\sim$100 km, while the PIXIE spectra are valid in the upper D region and lower E region, i.e., below $\sim$125 km.

PIXIE data are needed to capture the high-energy tail of the precipitating electrons. For those situations with very soft precipitation, additional information from other remote sensing techniques that work for $\bar{E}$ below 2 keV is needed.

References

Aksnes, A. (2005), Ionospheric global conductances derived from remote sensing of UV and X-ray emissions, Ph.D. thesis, Univ. of Bergen, Bergen, Norway.

Aksnes, A., J. Stadsnes, J. Bjordal, N. Østgaard, R. R. Vondrak, D. L. Detrick, T. J. Rosenberg, G. A. Germany, and D. Chenette (2002), Instantaneous ionospheric global conductance maps during an isolated substorm, *Ann. Geophys.*, *20*, 1181.

Aksnes, A., J. Stadsnes, G. Lu, N. Østgaard, R. R. Vondrak, D. L. Detrick, T. J. Rosenberg, G. A. Germany, and M. Schulz (2004), Effects of energetic electrons on the electrodynamics in the ionosphere, *Ann. Geophys.*, *22*, 475.

Aksnes, A., O. Amm, J. Stadsnes, N. Østgaard, G. A. Germany, R. R. Vondrak, and I. Sillanpää (2005), Ionospheric conductances derived from satellite measurements of auroral UV and X-ray emissions, and ground-based electromagnetic data: A comparison, *Ann. Geophys.*, *23*, 343.

Amm, O. (1995), Direct determination of the local ionospheric Hall conductance distribution from two-dimensional electric and magnetic field data: Application of the method using models of typical ionospheric electrodynamic situations, *J. Geophys. Res.*, *100*, 24,173.

Amm, O. (1998), Method of characteristics in spherical geometry applied to a Harang-discontinuity situation, *Ann. Geophys.*, *16*, 413.

Banks, P. M., and A. F. Nagy (1970), Concerning the influence of elastic scattering upon photoelectron transport and escape, *J. Geophys. Res.*, *75*, 1902.

Banks, P. M., C. R. Chappell, and A. F. Nagy (1974), A new model for the interaction of auroral electrons with the atmosphere: Spectral degradation, backscatter, optical emission, and ionization, *J. Geophys. Res.*, *79*, 1459.

Berger, M. J., S. M. Seltzer, and K. Maeda (1974), Some new results on electron transport in the atmosphere, *J. Atmos. Terr. Phys.*, *36*, 591.

Brittnacher, M., R. Elsen, G. Parks, L. Chen, G. Germany, and J. Spann (1997), A dayside auroral energy deposition case study using the Polar Ultraviolet Imager, *Geophys. Res. Lett.*, *24*, 991.

Christensen, T., N. Østgaard, T. J. Rosenberg, D. L. Detrick, G. A. Germany, and P. Stauning (2003), Conjugate high-intensity energetic electron precipitation at high latitude, *Ann. Geophys.*, *21*, 1443.

Chua, D., G. Parks, M. Brittnacher, W. Peria, G. Germany, J. Spann, and C. Carlson (2001), Energy characteristics of auroral electron precipitation: A comparison of substorms and pressure pulse related auroral activity, *J. Geophys. Res.*, *106*, 5945–5956.

Doe, R. A., J. D. Kelly, D. Lummerzheim, G. K. Parks, M. J. Brittnacher, G. A. Germany, and J. Spann (1997), Initial comparison of POLAR UVI and Sondrestrom IS radar estimates for auroral electron energy flux, *Geophys. Res. Lett.*, *24*, 999.

Germany, G. A., G. K. Parks, M. Brittnacher, J. Cumnock, D. Lummerzheim, J. F. Spann, L. Chen, P. G. Richards, and F. J. Rich (1997), Remote determination of auroral energy characteristics during substorm activity, *Geophys. Res. Lett.*, *24*, 995.

Germany, G. A., G. K. Parks, M. Brittnacher, J. F. Spann, J. Cumnock, D. Lummerzheim, F. J. Rich, and P. G. Richards (1998a), Energy characterization of a dynamic auroral event using GGS UVI images, in *Geospace Mass and Energy Flow: Results from the International Solar-Terrestrial Physics Program, Geophys. Monogr. Ser.*, vol. 104, edited by J. L. Horwitz, D. L. Gallagher, and W. K. Peterson, p. 143, AGU, Washington, D. C.

Germany, G. A., J. F. Spann, G. K. Parks, M. Brittnacher, R. Elsen, L. Chen, D. Lummerzheim, and M. Rees (1998b), Auroral observations from the Polar Ultraviolet Imager (UVI), in *Geospace Mass and Energy Flow: Results from the International Solar-Terrestrial Physics Program, Geophys. Monogr. Ser.*, vol. 104, edited by J. L. Horwitz, D. L. Gallagher, and W. K. Peterson, p. 149, AGU, Washington, D. C.

Germany, G. A., D. Lummerzheim, and P. G. Richards (2001), Impact of model differences on quantitative analysis of FUV auroral emissions: Total ionization cross sections, *J. Geophys. Res.*, *106*, 12,837.

Gledhill, J. A. (1986), The effective recombination coefficient of electrons in the ionosphere between 50 and 150 km, *Radio Sci.*, *21*, 339.

Grün, A. E. (1957), Lumineszenz-photometrische Messungen der Energie-Absorption im Strahlungsfeld von Elektronquellen, Eindimensionaler Fall in Luft, *Z. Naturforsch., Ser. A*, *12*, 89.

Imhof, W. L., et al. (1995), The Polar Ionospheric X-ray Imaging Experiment (PIXIE), *Space Sci. Rev.*, *71*, 385.

Inhester, B., J. Untiedt, M. Segatz, and M. Kürschner (1992), Direct determination of the local ionospheric Hall conductance distribution from two-dimensional electric and magnetic field data, *J. Geophys. Res.*, *97*, 4073.

Lorence, L. J. (1992), CEPXS/ONELD Version 2.0: A discrete ordinates code package for general one-dimensional coupled electron-photon transport, *IEES Trans. Nucl. Sci.*, *39*, 1031.

Lummerzheim, D., M. Brittnacher, D. Evans, G. A. Germany, G. K. Parks, M. H. Rees, and J. F. Spann (1997), High time resolution study of the hemispheric power carried by energetic electrons into the ionosphere during the May 19/20, 1996 auroral activity, *Geophys. Res. Lett.*, *24*, 987.

Mæhlum, B., and J. Stadsnes (1967), Scattering and absorption of fast electrons in the upper atmosphere, *Phys. Norvegica*, *2*, 111.

Nagy, A. F., and P. M. Banks (1970), Photoelectron fluxes in the ionosphere, *J. Geophys. Res.*, *75*, 6260.

Østgaard, N., J. Stadsnes, J. Bjordal, R. R. Vondrak, S. A. Cummer, D. Chenette, M. Schulz, and J. Pronko (2000), Cause of the localized maximum of X-ray emission in the morning sector: A comparison with electron measurements, *J. Geophys. Res.*, *105*, 20,869.

Østgaard, N., J. Stadsnes, J. Bjordal, G. A. Germany, R. R. Vondrak, G. K. Parks, S. A. Cummer, D. Chenette, and J. Pronko (2001), Auroral

electron distributions derived from combined UV and X-ray emissions, *J. Geophys. Res.*, *106*, 26,081.

Østgaard, N., G. A. Germany, J. Stadsnes, and R. R. Vondrak (2002a), Energy analysis of substorms based on remote sensing techniques, solar wind measurements and geomagnetic indices, *J. Geophys. Res.*, *107*(A9), 1233, doi:10.1029/2001JA002002.

Østgaard, N., R. R. Vondrak, J. M. Gjerloev, and G. A. Germany (2002b), A relation between the energy deposition by electron precipitation and geomagnetic indices during substorms, *J. Geophys. Res.*, *107*(A9), 1246, doi:10.1029/2001JA002003.

Rees, M. H. (1963), Auroral ionization and excitation by incident energetic electrons, *Planet. Space Sci.*, *11*, 1209.

Rees, M. H., and D. Lummerzheim (1989), Characteristics of auroral electron precipitation derived from optical spectroscopy, *J. Geophys. Res.*, *94*, 6799.

Richards, P. G., and D. G. Torr (1990), Auroral modeling of the 3371 Å emission rate: Dependence on characteristic electron energy, *J. Geophys. Res.*, *95*, 10,337.

Richmond, A. D. (1995a), Ionospheric electrodynamics, in *Handbook of Atmospheric Electrodynamics*, vol. II, edited by H. Volland, p. 249, CRC Press, Boca Raton, Fla.

Robinson, R. M., and R. R. Vondrak (1994), Validation of techniques for space based remote sensing of auroral precipitation and its ionospheric effects, *Space Sci. Rev.*, *69*, 331.

Robinson, R. M., R. R. Vondrak, J. D. Craven, L. A. Frank, and K. Miller (1989), A comparison of ionospheric electron densities and auroral luminosities observed simultaneously with the Chatanika radar and the DE-1 auroral imagers, *J. Geophys. Res.*, *94*, 5382.

Robinson, R. M., et al. (1992), Coordinated measurements made by the Sondrestrom radar and the Polar Bear ultraviolet imager, *J. Geophys. Res.*, *97*, 2863.

Sætre, C., J. Stadsnes, H. Nesse, A. Aksnes, S. M. Petrinec, C. A. Barth, D. N. Baker, R. R. Vondrak, and N. Østgaard (2004), Energetic electron precipitation and the NO abundance in the upper atmosphere: A direct comparison during a geomagnetic storm, *J. Geophys. Res.*, *109*, A09302, doi:10.1029/2004JA010485.

Semeter, J., D. Lummerzheim, and G. Haerendel (2001), Simultaneous multispectral imaging of the discrete aurora, *J. Atmos. Terr. Phys.*, *63*, 1981.

Sillanpää, I. (2002), One-dimensional method of characteristics to determine ionospheric conductances and currents, Ph.D. thesis, Finnish Meteorol. Inst., Helsinki, Finland.

Solomon, S. C. (1989), Auroral excitation of the N_2 2P (0,0) and VK (0,9) bands, *J. Geophys. Res.*, *94*, 17,215.

Solomon, S. C. (1993), Auroral electron transport using the Monte Carlo method, *Geophys. Res. Lett.*, *20*, 185.

Solomon, S. C., P. B. Hays, and V. J. Abreu (1988), The auroral 6300 Å emission: Observations and modeling, *J. Geophys. Res.*, *93*, 9867.

Strickland, D. J., D. L. Book, T. P. Coffey, and J. A. Fedder (1976), Transport equation techniques for the deposition of auroral electrons, *J. Geophys. Res.*, *81*, 2755.

Strickland, D. J., J. R. Jasperse, and J. A. Whalen (1983), Dependence of auroral FUV emissions on the incident electron spectrum and neutral atmosphere, *J. Geophys. Res.*, *88*, 8051.

Torr, M. R., et al. (1995), A far ultraviolet imager for the international solar-terrestrial physics mission, *Space Sci. Rev.*, *71*, 329.

Vickrey, J. F., R. R. Vondrak, and S. J. Matthews (1982), Energy deposition by energetic particles and Joule dissipation in the auroral ionosphere, *J. Geophys. Res.*, *87*, 5184.

Vondrak, R. R., and M. J. Baron (1976), Radar measurements of the latitudinal variation of auroral ionization, *Radio Sci.*, *11*, 939.

Vondrak, R. R., and R. Robinson (1985), Inference of high-latitude ionization and conductivity from AE-C measurements of auroral electron fluxes, *J. Geophys. Res.*, *90*, 7505.

Vondrak, R. R., R. M. Robinson, P. F. Mizera, and D. J. Gorney (1988), X-ray spectrophotometric remote sensing of diffuse auroral ionization, *Radio Sci.*, *23*, 537.

Walt, M., W. M. MacDonald, and W. E. Francis (1967), Penetration of auroral electrons into the atmosphere, in *Physics of the Magnetosphere*, edited by R. L. Carovillano, J. F. McClays, and H. R. Radoski, p. 534, Springer, New York.

—————————

A. Aksnes, Florida Space Institute, MS-FSI, Kennedy Space Center, FL 32899, USA. (aaksnes@mail.ucf.edu)

A. Brekke and U. P. Løvhaug, Department of Physics, University of Tromsø, 9037 Tromsø, Norway. (asgeir.brekke@phys.uit.no; unni.pia.lovhaug@phys.uit.no)

G. A. Germany, Center for Space Plasma and Astronomy Research, University of Alabama in Huntsville, Huntsville, AL 35899, USA. (germanyg@email.uah.edu)

K. Oksavik, Johns Hopkins University Applied Physics Laboratory, 11100 Johns Hopkins Road, Laurel, MD 20723, USA. (kjellmar.oksavik@jhuapl.edu)

N. Østgaard and J. Stadsnes, Department of Physics and Technology, University of Bergen, Allegt. 55, 5007 Bergen, Norway. (nikost@ift.uib.no; johan.stadsnes@ift.uib.no)

R. R. Vondrak, NASA Goddard Space Flight Center, Greenbelt, MD 20771, USA. (richard.r.vondrak@nasa.gov)